

Epitaxial growth and electrical-optical characteristics of CaAl_2Se_4 layers by hot-wall deposition technique

Jun Woo Jeong^a, Kwang Joon Hong^{a,*}, Jin Ju Bang^a, Ki Jung Lee^a, Kyung A Jeong^a, Tae Soo Jeong^b and Chang Joo Youn^b

^aDepartment of Physics, Chosun University, Gwangju 61452, South Korea

^bSchool of Semiconductor and Chemical Engineering, Semiconductor Physics Research Center (SPRC), Chonbuk National University, Jeonju 54896, South Korea

The epitaxial CaAl_2Se_4 (CAS) layers were first grown through the hot-wall deposition technique with an attached reservoir tail. The coincidence lattice mismatch between the CAS layer and the GaAs substrate was found to be -0.25% as a result of the compressive strain. From the relation between the reciprocal temperature and the carrier concentration, the donor level originating from slight stoichiometric deviations were extracted to be 1.77, 20.06, and 93.72 meV below the conduction band. Thus, from a log-log plot between the mobility and the temperature, at the high temperatures above 90 K, the electron mobility showed a temperature dependence of two different types. One was $T^{1/2}$ at the temperature range of $90 < T < 220$ K and the other was $T^{3/2}$ at the temperatures of $T > 220$ K. The former is the scattering due to the acoustic phonon mode of lattice vibration, and the latter is due to the piezoelectric potential scattering. While, at the low temperatures below 90 K, the mobility decreased in proportion to T^1 . And its decrease is attributed to the dislocation scattering. From the photocurrent (PC) spectroscopy, we found that the characteristic PC peaks were originated by the band-to-band transitions. The temperature-dependent band-gap variation was well explained by $E_g(T) = E_g(0) - 4.94 \times 10^{-3} T^2 / (T + 552)$, where $E_g(0)$ is estimated to be 3.8239, 3.8716, and 3.8801 eV. Consequently, low-temperature growth of the epitaxial CAS layers was successfully achieved by using the hot-wall deposition technique.

Key words: Characterization, Hot wall epitaxy, Calcium compounds, Semiconducting ternary compounds.

Introduction

$\text{XAl}_2(\text{S}, \text{Se})_4$ ternary compounds basing on alkaline earth metals ($\text{X} = \text{Mg}, \text{Ca}, \text{Sr}, \text{and Ba}$) are interesting materials because they have a various physical characteristics of wide band gap, wide transparency intervals, high photoconductivity, and strong luminescence [1-4]. Therefore, it can be applied for optoelectronic devices operating in blue and ultraviolet wavelength regions. In order to achieve the best performance in the device, it is required to grow high quality crystals. However, the high quality growth on the ternary compounds containing alkaline earth metals is not easy because of their very high melting points [5]. Therefore, a non-stoichiometry is formed in the crystal due to the growing process and additional thermal treatment. Also, it promotes the generation of the native defects (vacancies, interstitials, and these complexes), which contributes to self compensation. These facts denote the difficulty of the stoichiometric growth on these ternary compounds. Especially,

calcium aluminum selenide (CaAl_2Se_4 : CAS) of these ternary compounds is not easy to obtain high quality crystal. Al element has a low miscibility in ternary compound [6], so there is a possibility of causing Al-rich cluster region in the crystal or forming the intermetallic CaAl_4 with Ca element [7, 8]. Furthermore, the partial vapor pressure of Se is higher than the vapor pressure of Ca and Al elements when CAS is synthesized. It can change chemical composition ratio of the crystals, thus it gives rise to native defects and self-compensation. To suppress these detective defects, the low-temperature growth method is required. The hot-wall epitaxy (HWE) method [9], which has been used to grow a high-purity ZnSe epilayer at a low temperature [10], is one of the low-temperature crystal-growth technologies. Thus, the HWE system has been especially designed to grow epilayers under conditions of near thermodynamic equilibrium [11]. HWE is operated as semiclosed growth reactor, consisting of a vertically mounted quartz cylinder, which is controlled by three heat stages and is closed on top by the substrate. The growth of the CAS epilayer through the HWE technique, however, was rarely reported before now.

In this study, the growth of the epitaxial CAS layers on the GaAs substrate was first conducted through the HWE technique. The characterization of the CAS

*Corresponding author:
Tel : +82-62-230-6637
Fax: +82-62-234-4326
E-mail: kjhong@chosun.ac.kr

layers was investigated by using double crystal X-ray diffraction (DCXD), atomic force microscopy (AFM), Hall effect, optical absorption (OA), and photocurrent (PC) measurements. Based on these results, the structural, electrical, and optical properties were discussed as a function of temperature.

Experimental Procedure

To synthesize the polycrystal ingot of CAS, 6 N-purity shot-types of Ca, Al, and Se (all from Aldrich) were weighed according to the stoichiometric proportions. Then, the weighed elements were sealed in evacuated quartz tubes. Fig. 1 presents the furnaces used for the polycrystalline and the layer growth of CAS. Fig. 1(a) is the horizontal furnace of the Bridgman method designed for the polycrystal synthesis. As shown in Fig. 1(a), the sealed ampoule was placed in the synthesis furnace and was continually rotated at a rate of 1 revolution per minute. In order to prevent an explosion of the ampoule due to the high partial pressure of Se, we gradually increased the temperature of the ampoule to 500 °C and then maintained that temperature for 24 hrs. While the ampoule was vibrated to the left and right, its temperature was increased gradually to 1050 °C. Thereafter, the temperature was kept for 48 hrs. After these processes, a colorless-transparent CAS ingot was synthesized.

Fig. 1(b) is the HWE apparatus used for the layer growth with the polycrystal ingot of CAS. This HWE apparatus constructed by the electric furnaces of three stages was made of a quartz tube with Kanthal wire. A substrate holder is located in the furnace between the first stage labeled as a substrate and the second stage labeled as a source. Here, one of the roles of the substrate holder serves as a lid to close the top of the source tube. And the reservoir stage is posited at the bottom of the vertical quartz tube and its purpose is to uniformly maintain the total partial pressures on each element in the quartz tube. Each part of the quartz tube is connected to the temperature controller, so as to independently control the temperature of each quartz

tube. At this time, the HWE source-materials were prepared by the polycrystal CAS ingot and an undoped semi-insulating GaAs (001) wafer was used as substrates for HWE growth. Here, the GaAs (001) phase is the favored growth substrate, partly because of the ease with which it may be cleaned and partly because of the difficulty of achieving good HWE growth on other phases such as (111) [12]. The substrate was cleaned ultrasonically for 1 min in successive baths of trichloroethylene, acetone, methanol, and 2-propanol and etched for 1 min in a solution of $\text{H}_2\text{SO}_4:\text{H}_2\text{O}_2:\text{H}_2\text{O}$ (5 : 1 : 1). The substrate was degreased in organic solvents and rinsed with deionized water (18.2 MW). After the substrate was dried off, the substrate was immediately loaded onto the substrate holder in the HWE apparatus and was annealed at 580 °C for 20 min to remove the residual oxide on the surface of the substrate.

The structure and surface morphology of the grown CAS layers were analyzed by DCXD and AFM measurements. In order to take Hall effect and PC measurements, Au electrodes with a coplanar geometry were fabricated on the CAS layer by using an e-beam evaporator and confirmed Ohmic contacts of the electrodes by using current-voltage measurements. Especially, the distance between electrodes of PC specimen was 1.5 mm. Then, a bias of 2 V was applied to the circuit. The PC measurement was done while the monochromatic light emitted from a xenon lamp (Output power: 500 W) was illuminated on the specimens. At this time, the monochromatic light was normalized, and its intensity was $18 \mu\text{W}/\text{cm}^2$. Also, OA device using an ultraviolet visible near-infrared (UV-VIS-NIR) spectrophotometer (Hitachi, U-3501) was used to measure the band gap energy. These measurements were done while varying the temperature from 10 to 293 K.

Results and Discussion

Growth and structural property

Fig. 2 shows the diffraction patterns of CAS polycrystal measured through the X-ray diffraction (XRD) method. Through the JCPDS (Joint Committee on Powder Diffraction Standards) card, it was found that the synthesized CAS polycrystal crystallized into an orthorhombic structure. By using the extrapolation method, the lattice constants of a_0 , b_0 , and c_0 were found to be 6.3252, 10.4713, and 10.5271 Å, respectively. These lattice constants are in good agreement with the values reported by Klee and Schäfer [2].

The ingot of the synthesized CAS polycrystal was used as a source material in HWE apparatus when the layer grows. At this time, the heating temperature of the source part was determined to 600 °C throughout the experimental repetition process. The temperature of the reservoir is decided from a partial vapor pressure of the source maintained at P_{min} , which is identified to the minimum value of the total pressure in the chamber

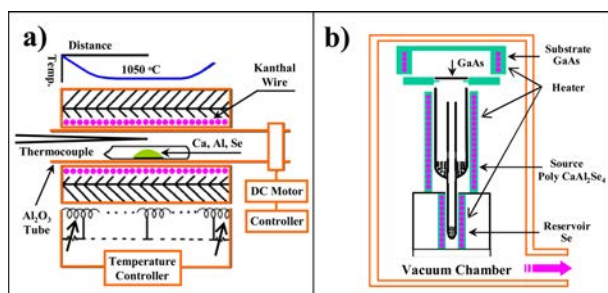


Fig. 1. The furnaces used for the polycrystalline and the layer growth of CAS: (a) the horizontal furnace of the Bridgman method designed for the polycrystal synthesis, (b) the HWE apparatus used for the layer growth with the polycrystal ingot of CAS.

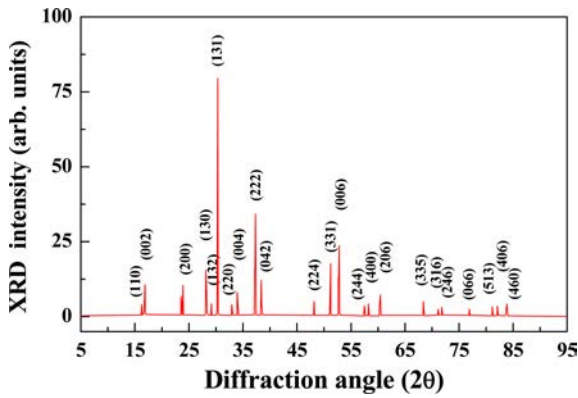


Fig. 2. XRD curves of polycrystalline CAS.

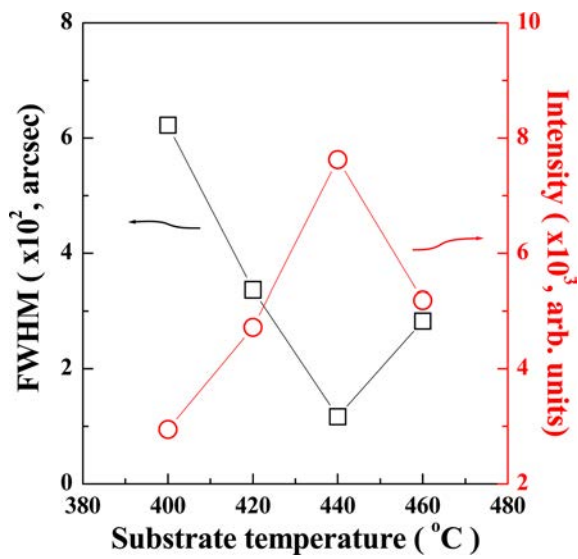


Fig. 3. Intensity and HWHM values of the DCXD rocking curve as a function of substrate temperature.

[13]. And, the vapor pressure of the reservoir is given as a $1/3P_{\min}$ if the reservoir material is a nonmetallic element. Therefore, when P_{\min} is about 10^{-1} Torr during the growth, the vapor pressure of the reservoir is estimated to be about 10^{-2} Torr. About reservoir tube filled with Se elements, its temperature was extracted to be 245 °C. Under these conditions, the CAS layers were grown when the substrate temperature varied to 400, 420, 440, and 460 °C.

Fig. 3 presents the full width at half maximum (FWHM) and the intensity of DCXD measured as a function of substrate temperature. DCXD experiment conducted to find the optimum growth parameter. As Fig. 3 shows, FWHM of the 440 °C layer was a lowest value and its intensity was a highest. The minimum FWHM value means that the grown layer becomes an epitaxial layer of high quality. Therefore, this fact indicates that the optimum substrate temperature is 440 °C. From these results, the optimum growth temperatures of source, substrate, and reservoir were found to be 600, 440, and 245 °C, respectively. Furthermore, the thickness and the growth rate of the layer grown under these conditions

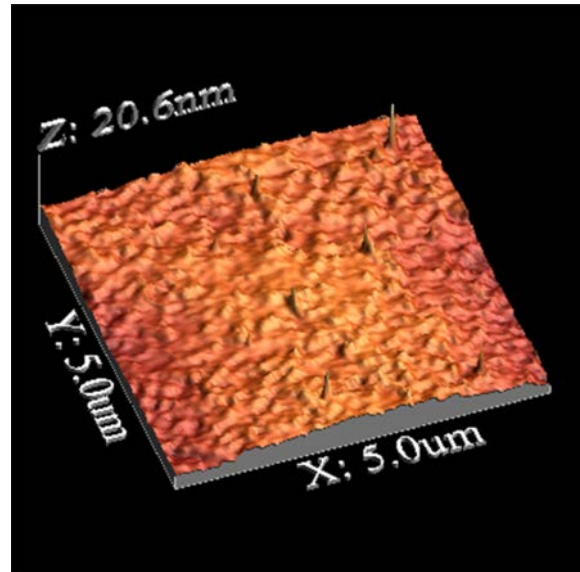


Fig. 4. AFM-surface morphology of the CAS layer.

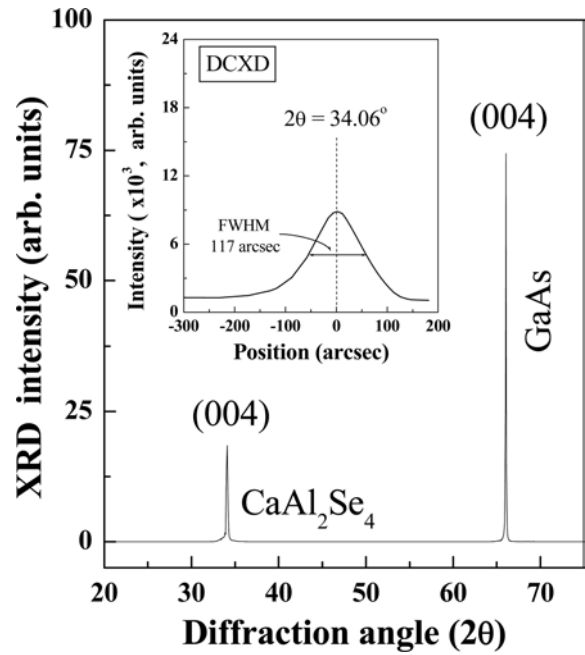


Fig. 5. XRD and DCXD rocking curves on the epitaxial CAS layers grown at the optimum substrate temperature of 440 °C.

were obtained to be 2.2 μm and 1.11 $\text{\AA}/\text{s}$, respectively. Fig. 4 displays the AFM-surface morphology of the CAS layer grown below optimum growth conditions. As shown in Fig. 4, the surface morphology of the grown layer was smooth. The root-mean-square roughness, Rms, of the surface was 1.31 nm. It suggests that the smooth surface and the low Rms value are attributed to low growth rate of 1.11 $\text{\AA}/\text{s}$. Such a low growth rate is one of the many benefits of having the HWE method.

Fig. 5 shows the XRD and DCXD spectra of the CAS layers obtained under the optimum growth condition maintaining the optimal temperatures of

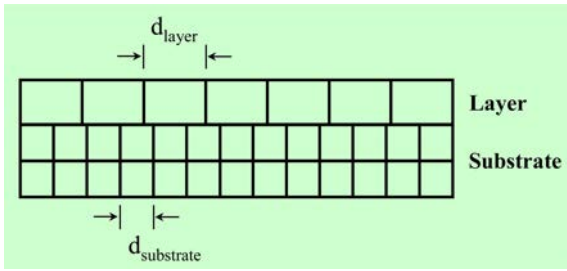


Fig. 6. A simple lattice model with CLS between the layer and the substrate.

source 600, substrate 440, and reservoir 245 °C. As Fig. 5 shows, only two peaks were observed in XRD rocking curve. One peak is the (004) plane of the grown CAS layer and another one corresponds to the (004) plane of the GaAs substrate wafer. Thus, other diffraction peak except two peaks was not observed in Fig. 5. Here, the CAS (004) peak was posited at 34.06°. It indicates that the grown CAS layer is crystallized into the orthorhombic structure. Also, the large distance difference between two peaks means to be a phase separation having a lattice mismatch. At this time, the inter-planar spacing (d_{hkl}), which is the distance between crystallographic planes belonging to the family (hkl) on CAS (004) and GaAs (004), was extracted to be 2.6302 and 1.4128 Å, respectively. In fact, a large difference of the lattice between these materials is difficult to grow the epitaxial layer. Nevertheless, the difficulty of the high quality layer-growth due to the large lattice mismatch can be overcome by explaining a coincidence site lattice (CSL), which was reported by Trampert et al. [14]. Fig. 6 displays a simple lattice model with CLS between the layer and the substrate. The coincidence between the substrate and the layer lattices can be expressed by

$$md_{\text{substrate}} = nd_{\text{layer}} \quad (1)$$

where m and n are integers meaning CSL between the substrate and the layer, respectively. Also, m and n are given to a pair of integers (m, n). Therefore, the substrate and the layer having lattice spacing close to an integer ratio m/n may form an epitaxial interface described by a coincidence lattice [15, 16]. The coincidence lattice mismatch δ , which expressed the deviation from true coincidence, is given by

$$\delta\% = \frac{md_{\text{substrate}} - nd_{\text{layer}}}{md_{\text{substrate}}} \times 100 \quad (2)$$

Here, positive or negative values of δ give rise to a tensile strain or compressive strain in the layer, respectively. According to Eq. (1), every seventh CAS (004) plane corresponds to every thirteenth GaAs (004) plane. By using Eq. (2), when the integers (m, n) is (13, 7), the δ value was reduced to -0.25%. This result is a reasonable value for the epitaxial growth. Furthermore,

it found that the CAS layer was influenced by the compressive strain due to negative value of δ during the layer growth. As shown in the inset of Fig. 5, the DCXD curve of the CAS (004) phase was measured and its FWHM was a 117 arcsec. This DCXD observation implies that the grown layer is a high quality crystal, because it is not easy to observe DCXD spectrum from the low quality crystal. Consequently, the grown CAS layer was epitaxially grown along the (004) direction on to the GaAs (004) substrate.

Temperature-dependent electron concentration and mobility

Fig. 7 displays the electron concentration and mobility as a function of temperature T . For n -type semiconductors, the concentration of electron carriers in the conduction band can be expressed as:

$$n = n_0 \exp(-E_D/kT) \quad (3)$$

where n_0 is a constant and E_D is the thermal activation energy. From the relationship between the reciprocal temperature and the electron concentration by Eq. (3), three activation energies were observed at the deep level of 93.72 meV in the high temperature range and the shallow levels of 20.06 in the middle temperature range and 1.77 meV in the low temperature range, as shown in Fig. 7(a). At this time, the behavior of the carriers in the low temperature range was less temperature dependent. These activation energies indicate the existence of the donor levels being below the conduction band edge. Al atoms commonly form more covalent bonds than Ca and Se atoms in structure. Thus, Al atoms participate in the formation of pre-covalent and less ionic structures than Ca and Se atoms. Consequently, Al atoms can exist as a stable element in CAS. Thereby, the capable native defects must be related to Ca interstitials (Ca_{int}), Se vacancies (V_{Se}), and/or combinations of these. Also, it suggests that these donor levels are originated by slight stoichiometric deviations.

On the other hand, by introducing Matthiessen's rule, the total electron mobility μ in n -type semiconductor is given by

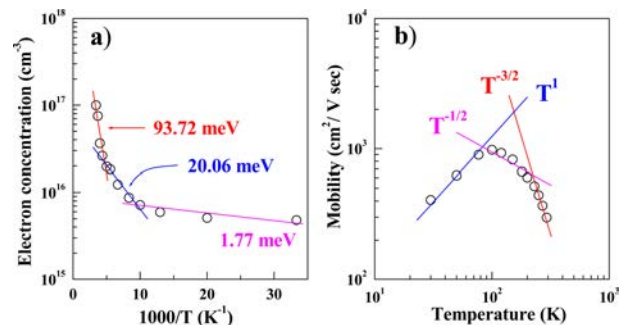


Fig. 7. Electron concentration (a) and mobility (b) as a function of temperature T .

$$1/\mu = 1/\mu_{\text{phonon}} + 1/\mu_{\text{impurity}} \quad (4)$$

where μ_{phonon} and μ_{impurity} are the mobilities of the phonon and the impurity, respectively. Here, there are two prominent scattering mechanisms limiting the mobility of carriers in the layer of phonon scattering (lattice scattering) and impurity scattering [17]. Lattice scattering comes from thermal vibrations due to the thermal agitation of the lattice atoms in the layer. These vibrations disturb the lattice periodic potential and allow energy to be transferred between the carriers and the lattice. Thus, lattice scattering becomes dominant at high temperatures; the mobility decreases with increasing temperature. This effect can be qualitatively understood as phonons colliding with charge carriers. Thereby, the lattice scattering is attributed to three phonons of the deformation potential acoustic phonons, piezoelectric acoustic phonons, and polar optical phonons. Therefore, the mobility dominated by acoustic phonon interaction is expected to be proportional to $T^{-3/2}$. Also, the mobility due to piezoelectric acoustic phonons scattering is expected to be proportional to $T^{-1/2}$. On the other hand, impurity scattering takes place when a charge carrier travels past the ionized dopant impurity. Ionized dopant impurity scattering emerges from the dopants of background donors, surface donors and dislocations. However, scattering by dislocations becomes less significant at higher temperatures, where the mobility increases with increasing temperature. As shown in Fig. 7(b), the mobility tended to increase with increasing temperature up to 90 K, after which it decreased. In the high temperature range of $T > 220$ K, the mobility is proportional to $T^{-3/2}$. It implies that the scattering is mainly caused by the acoustic phonon mode of lattice vibrations through a deformation potential [17]. Thus, at the intermediate temperature range of $90 < T < 220$ K, the mobility gradually decreases as a function of $T^{-1/2}$ with increasing temperature. Such a behavior is attributed to piezoelectric potential scattering, which varies as $T^{-1/2}$ [18]. Consequently, it found out that the mobility at temperatures over 90 K was governed by the combined scattering due to piezoelectric and deformation acoustic phonons while the mobility in the low temperature range of $T < 90$ K is proportional to T^1 . This scattering can be described as dislocation scattering, which is caused by the change of dislocation in the layer [19].

Spectral PC analysis

For light with a variable photon energy (E_p) near the band gap energy (E_g), light with lower-energy photons ($E_p < E_g$) is transmitted without being absorbed and light with higher-energy photons ($E_p > E_g$) is absorbed. The strongly-absorbed excitation creates a high density of free electron-hole pairs (EHPs) near the surface. Ultimately, EHPs generation is used to designate the valence-band electron as part of a covalent bond [20]. Therefore, when the covalent bond is broken, the

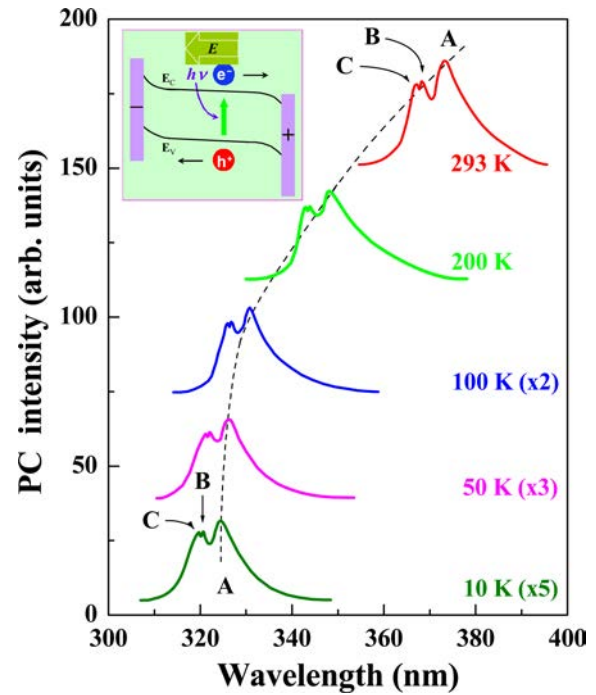


Fig. 8. Characteristic PC spectra of the CAS layer measured at the several temperatures. Here the dotted line represents the peak A obtained at each the temperature. Also, the subfigure displays the band-bending structure of PC generated in the layer on exposure to light as an electric field was applied.

electron is free to move in the crystal lattice of the layer. The required energy to break a covalent bond is E_g . If the photon energy is $E_p < E_g$, it is not sufficient to break a covalent bond and free an electron for conduction. At this time, electrons do not occupy the forbidden states between the valence and the conduction bands, so a photon with $E_p < E_g$ is not absorbed and passes through the layer. Therefore, for a typical photosensitive layer, the lifetime for surface excitation of $E_p > E_g$ is much shorter than the lifetime for volume excitation of $E_p < E_g$. Consequently, the PC measurement is related to the absorption of photons, leading to the generation of free charge particles in the conduction band and/or in the valence band.

Fig. 8 presents the PC spectra of the epitaxial CAS layer obtained at the several temperatures. Also, the subfigure in Fig. 8 is the band-bending structure of PC generated in the layer on exposure to light as an electric field was applied. As shown in the subfigure, absorbed photons with higher energy than the band gap energy create electron and hole carriers in the conduction and valence bands, respectively. These electron and hole carriers instantly flow through the anode and cathode, respectively, owing to the electric field caused by the bias voltage. Consequently, these carriers, which flow toward the electrodes, produce a PC signal. A PC response is indicative of an electron transition from the valence band to the conduction band. At this time, a maximum peak in the PC spectrum occurs when a

transition is made from surface excitation to volume excitation with increasing wavelength [21]. This maximum PC peak means the band gap due to the band-to-band transition [21, 22]. As Fig. 8 shows, three dominant peaks observed at total temperature region from 10 to 293 K. At 293 K, three PC peaks were located to 373.2 (3.3222), 367.9 (3.3701), and 366.9 nm (3.3793 eV). These peaks were labeled as peaks A, B, and C to indicate the transitions from the three valence-band levels in order of increasing energy, respectively. At this time, appearance of three PC peaks comes from the result, which lifted by the combined influences of spin-orbit interaction and the noncubic crystalline field [23]. Thus, these PC peaks are attributed to the transition of electrons from the valence band to the conduction band. So, they mean each direct band gap transition from the three valence-band levels. Therefore, these PC peaks correspond to band-to-band transitions. The peaks A, B, and C at 10 K were also observed at 323.3 (3.8232), 320.3 (3.8709), and 319.6 nm (3.8794 eV), respectively.

On the other hand, the PC slope toward the longer wavelength region of the spectrum is related to the crystal quality. If there are the optically active traps, then it takes along time to attain a steady-state value after the monochromatic light is vanished. Ultimately, PC response will be observed to a rough spectrum. Furthermore, the spectral PC response caused by the defect states is extended to longer wavelengths and it will be observed as a rough spectrum. So, the presence of a defect state in the layer perturbs or alters the recombination process [21]. At this time, the defect states include vacancies, interstitial atoms, or dislocations, etc. As Fig. 8 shows, the PC curve located to the long wavelength direction is a smooth gradient. Consequently, this fact implies that the grown epitaxial CAS layers are high quality crystal.

Temperature-dependent PC spectrum

The band gap for any semiconductor varies as functions of temperature and pressure. Therefore, the band gap variation can be expressed as [22]:

$$\Delta E_G = (\partial E_G / \partial P)_T \Delta P + (\partial E_G / \partial T)_P \Delta T \quad (5)$$

When $A = (\partial E_G / \partial T)_P$ and $B = (\partial E_G / \partial P)_T$, the band gap at constant pressure is $E_G = E_G(0) + AT$, where $E_G(0)$ is the band gap energy at 0 K. For most photoconductor materials, the value of A is a negative quantity. Therefore, the band gap as a function of temperature can be well matched by the Varshni's empirical equation [24, 25]:

$$E_g(T) = E_g(0) - aT^2 / (b + T) \quad (6)$$

where a and b are constants. Also, $E_g(0)$ is the band gap energy at 0 K.

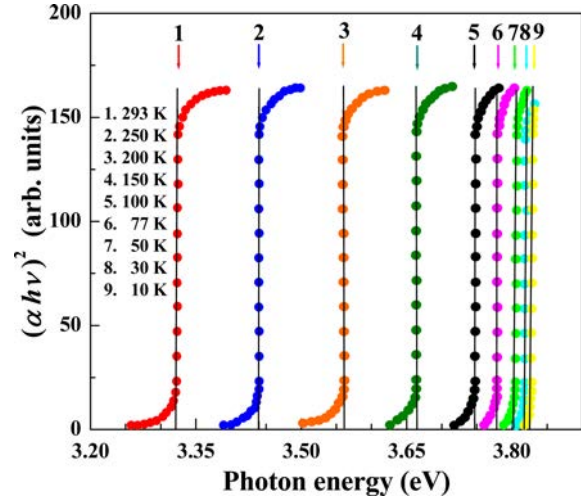


Fig. 9. Plots of $(\alpha h\nu)^2$ versus photon energy for different temperatures.

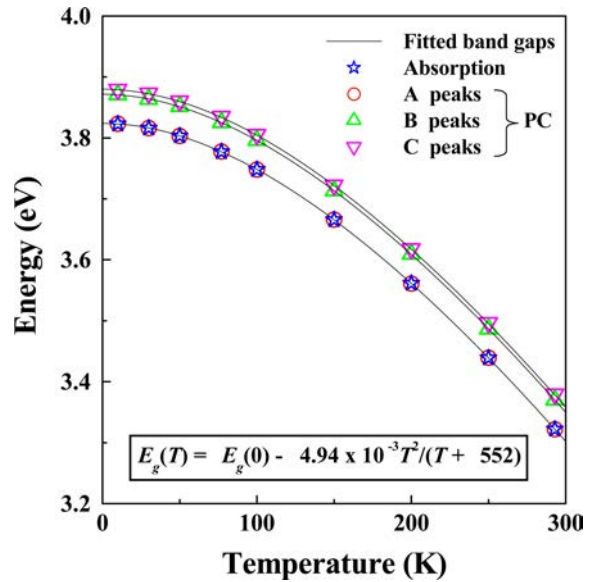


Fig. 10. Energy variation of the CAS layer, which was obtained from PC and OA measurements.

On the other hand, the band gap observation has been maintained by means of the OA coefficient measurement. When photons are incident on a material, the intensity of the transmitted photon is expressed by the Lambert-Beer-Bouguer law [26]:

$$I = I_0 \exp(-\alpha d) \quad (7)$$

where I_0 and I are the intensities of photon entering and leaving the layer, respectively. Also, a and d are OA coefficient and thickness of the layer, respectively. At this time, I is exponentially reduced while traveling through the layer and α is strongly depended to the incident photon energy ($h\nu$). Therefore, Eq. (7) is rewritten as

$$\alpha = - (1/d) \ln(I/I_0) \quad (8)$$

From the OA measurement, the relation between α and $h\nu$ was extracted from the OA spectra. The absorption coefficient as a function of photon energy in the allowed direct transition can be expressed as [27]

$$(\alpha h\nu)^2 = A(h\nu - E_g) \quad (9)$$

where h is the Planck constant and A is a constant because it do not involve phonons due to the lattice vibrations in electron band-to-band transitions. According to Eq. (9), $(\alpha h\nu)^2$ linearly depends on the photon energy. Fig. 9 shows the plots of $(\alpha h\nu)^2$ versus photon energy for different temperatures. As shown in Fig. 9, the optical band gap can be extracted by extrapolating the linear portions of the respective curves to zero [28].

Now, let's discuss the band gap results extracted from these PC and OA measurements. As Fig. 8 shows, three PC peaks trend of shifting toward the short-wavelength region with decreasing temperature and their energies correspond to band-to-band transitions. Fig. 10 displays the energy variation of the CAS layer, which was obtained from PC and OA measurements. As shown in Fig. 10, the energies of the PC-peak positions on the peak A are consistent with those obtained by OA spectroscopy at the same temperature. As a means for pursuing another technique for obtaining the band gap, it indicates that the band gap energy of the CAS layer can be well represented by the energy extracted by means of PC spectroscopy. Also, these energies increased with decreasing temperature and had a nonlinear relationship. By fitting Eq. (6), a and b are extracted out to be 4.94×10^{-3} eV/K and 552 K, respectively. Thus, $E_g(0)$ is estimated to 3.8239, 3.8716, and 3.8801 eV for the transitions corresponding to peaks A, B, and C, respectively. Under these conditions, three PC-peak energies are well satisfied with the Eq. (6). Furthermore, three PC peaks of A, B, and C correspond to $E_g(A)$, $E_g(B)$, and $E_g(C)$ in the valence band in order of increasing energy, respectively. At 10 K, the band gap energy of the epitaxial CAS layers is estimated to be 3.8230 eV. This value is in agreement with the 3.823 eV value obtained by OA measurement from the CAS single crystal at 10 K [29]. This fact indicates that PC measurement is one of the most useful methods for the band gap determination of the CAS layer because it can directly obtain the energy corresponding to the band gap by measuring the PC-peak position. In fact, the OA method has been known to be inaccurate for obtaining the band gap because of the difficulty in defining the position of the absorption edge. Consequently, the appearance of the PC peaks is attributed to the band-to-band transition from the valence band to the conduction band.

Conclusions

The epitaxial CAS layers were grown on GaAs

substrate by using the HWE method. The optimum growth temperatures on source, substrate, and reservoir extracted out to be 600, 440, and 245 °C, respectively. The thickness and growth rate were obtained to be 2.2 μm and 1.11 $\text{\AA}/\text{s}$, respectively. The grown CAS layer is crystallized into the orthorhombic structure. Thus, the layer was epitaxially accumulated along the (004) direction onto the GaAs (004) substrate and its FWHM of DCXD was 117 arcsec. According to the CSL model, the coincidence lattice mismatch was -0.25%, which is influenced by the compressive strain, with the integer pair of (13, 7).

From the relationship between the reciprocal temperature and the carrier concentration, three activation energies were observed, at the deep level of 93.72 meV in the high temperature range and the shallow levels of 20.06 in the middle temperature range and 1.77 meV in the low temperature range. These donor levels are caused by the native defects originating from slight stoichiometric deviations, which are Ca_{int} , V_{Se} , and/or combinations of these. From the temperature dependence of the Hall mobility, the electron mobility tended to increase with increasing temperature up to 90 K, after which it decreased. During increasing temperature to 90 K, the mobility increased as a function of T^1 and it was attributed to the dislocation scattering. At the higher temperature region than 90 K, the mobilities were decreased as the functions of $T^{-3/2}$ at $T > 220$ K and of $T^{-1/2}$ at $90 < T < 220$ K, respectively. The former was mainly caused by the scattering of the acoustic phonon mode of lattice vibrations through a deformation potential and the latter was owing to the piezoelectric potential scattering.

From the PC measurement, three PC peaks corresponding to the band-to-band transition were observed. It suggested that its origin was caused by the transition of electrons from the three valence band states in order of increasing energy, respectively, to the conduction band states, respectively. Thus, the PC peaks shifted toward the short wavelength region with decreasing temperature. These PC peaks was well analyzed by following $E_g(T) = E_g(0) - 4.94 \times 10^{-3} T^2 / (T + 552)$, where $E_g(0)$ is estimated to be 3.8239, 3.8716, and 3.8801 eV for the PC peaks A, B and C, respectively. This behavior was consistent with the results from OA measurements.

Acknowledgments

This study was supported by research funds from Chosun University, 2017.

References

1. M.-S. Jin, T.-Y. Park, H.-G. Kim, H.-G. Choe, H.-J. Song, S.-K. Oh and W.-T. Kim, J. Appl. Phys. 86 (1999) 6596-6598.
2. W. Klee and H. Schäfer, Z. Naturforsch. 33b (1978) 829-833.

3. S.H. You, K.J. Hong, T.S. Jeong and C.J. Youn, *J. Cryst. Growth* 419 (2015) 31-36.
4. P. Benalloul, C. Barthou, J. Benoit, L. Eichenauer and A. Zeinert, *Appl. Phys. Lett.* 63 (1993) 1954-1956.
5. http://www.secret-bases.co.uk/wiki/Alkaline-earth_oxide.
6. H. Serier, M. Gaudon and M. Menetrier, *Solid State Sci.* 11 (2009) 1192-1197.
7. <http://www.totalmateria.com/Article55.htm>.
8. D. Kevorkov and R. Schmid-Fetzer, *Z. Metallkd.* 92 (2001) 946-952.
9. H. Yang, A. Ishida, H. Fuiyasu and H. Kuwabara, *J. Appl. Phys.* 65 (1989) 2838-2842.
10. T.S. Jeong, P.Y. Yu, K.J. Hong, T.S. Kim, C.J. Youn, Y.D. Choi, K.S. Lee, B. O and M.Y. Yoon, *J. Cryst. Growth* 249 (2003) 9-14.
11. A. Lopez-Otero, *Thin Solid Films* 49 (1978) 3-57.
12. M.A. Herman and H. Sitter, *Molecular Beam Epitaxy: Fundamentals and Current Status*, (Springer, 1989).
13. M.R. Lorenz, *Physics and Chemistry of II-VI Compounds*, Eds. M. Aven, J.S. Prener, (North-Holland, 1967).
14. A. Trampert, O. Brandt and K.H. Ploog, Crystal structure of group III Nitrides, in: J.I. Pankove, T.D. Moustakas (Eds.), *Semiconductors and Semimetals*, Vol. 50, Academic, (San Diego, 1998).
15. A. Trampert, *Physica E* 13 (2002) 1119-1125.
16. A.P. Sutton and R.W. Balluffi, *Acta Metallurgica* 35 (1987) 2177-2201.
17. S.M. Sze, *Semiconductor Devices Physics and Technology*, (Wiley, 1985).
18. M.K. Hudait, Y. Lin, P.M. Sinha, J.R. Lindemuth and S.A. Ringel, *J. Appl. Phys.* 100 (2006) 063705.
19. K. Kusakabe, T. Furuzuki and K. Ohkawa, *Physica B* 376-377 (2006) 520-522.
20. <https://classes.soe.ucsc.edu/ee145/Spring02EE145Lab8.pdf>.
21. N.V. Joshi, *Photoconductivity: Art, Science, and Technology*, (Marcel Dekker, 1990).
22. R.H. Bube, *Photoconductivity of Solids*, (Wiley, 1969).
23. J.L. Shay and J.H. Wernick, *Ternary Chalcopyrite Semiconductors: Growth, Electronic Properties, and Applications*, (Pergamon, 1975).
24. Y.P. Varshni, *Physica* 34 (1967) 149-154.
25. D.-R. Hang, S. E. Islam, K.H. Sharma, S.-W. Kuo, C.-Z. Zhang and J.-J. Wang, *Nanoscale Res. Lett.* 9 (2014) 632.
26. N.M. Ahmed, Z. Sauli, U. Hashim and Y. Al-Douri, *Int. J. Nanoelectron. Mater.* 2 (2009) 189-195.
27. J.I. Pankove, *Optical Processes in Semiconductors*, (Dover, 1971).
28. B.C. Mohanty, D.H. Yeon, B.K. Kim and Y.S. Cho, *J. Electrochem. Soc.* 158 (2011) 30-35.
29. S.-K. Oh, H.-J. Song, W.-T. Kim, H.-G. Kim, C.-I. Lee, T.-Y. Park, M.-S. Jin and C.-D. Kim, *Semicond. Sci. Technol.* 15 (2000) 108-111.